Surfactant-Assisted Perovskite Nanofillers Incorporated in Quaternized Poly (Vinyl Alcohol) Composite Membrane as an Effective Hydroxide-Conducting Electrolyte

Selvaraj Rajesh Kumar [1], Wei-Ting Ma [1], Hsin-Chun Lu [1], Li-Wei Teng [1], Hung-Chun Hsu [1], Chao-Ming Shih [1], Chun-Chen Yang [2] and Shingjiang Jessie Lue [1,3,4,*]

[1] Department of Chemical and Materials Engineering, and Green Technology Research Center, Chang Gung University, Guishan District, Tao-yuan 333, Taiwan; rajeshkumarnst@gmail.com (S.R.K.); carherine81@gmail.com (W.-T.M.); hsinchun@mail.cgu.edu.tw (H.-C.L.); xz80919@hotmail.com.tw (L.-W.T.); b9923026@ems.niu.edu.tw (H.-C.H.); nanochitosan@gmail.com (C.-M.S.)

[2] Department of Chemical Engineering and Battery Research Center of Green Energy, Ming Chi University of Technology, New Taipei City 24301, Taiwan; ccyang@mail.mcut.edu.tw

[3] Department of Radiation Oncology, Chang Gung Memorial Hospital, Kwei-shan, Tao-yuan 333, Taiwan

[4] Department of Safety, Health and Environmental Engineering, Ming Chi University of Technology, New Taipei City 24301, Taiwan

* Correspondence: jessie@mail.cgu.edu.tw; Tel.: +886-3-2118800 (ext. 5489); Fax: +886-3-2118700

Abstract: Perovskite $LaFeO_3$ nanofillers (0.1%) are incorporated into a quaternized poly(vinyl alcohol) (QPVA) matrix for use as hydroxide-conducting membranes in direct alkaline methanol fuel cells (DAMFCs). The as-synthesized $LaFeO_3$ nanofillers are amorphous and functionalized with cetyltrimethylammonium bromide (CTAB) surfactant. The annealed $LaFeO_3$ nanofillers are crystalline without CTAB. The QPVA/CTAB-coated $LaFeO_3$ composite membrane shows a defect-free structure while the QPVA/annealed $LaFeO_3$ film has voids at the interfaces between the soft polymer and rigid nanofillers. The QPVA/CTAB-coated $LaFeO_3$ composite has lower methanol permeability and higher ionic conductivity than the pure QPVA and QPVA/annealed $LaFeO_3$ films. We suggest that the CTAB-coated $LaFeO_3$ provides three functions to the polymeric composite: increasing polymer free volume, ammonium group contributor, and plasticizer to enhance the interfacial compatibility. The composite containing CTAB-coated $LaFeO_3$ results in superior cell performance. A maximum power density of 272 mW cm^{-2} is achieved, which is among the highest power outputs reported for DAMFCs in the literature.

Keywords: $LaFeO_3$ nanoparticles; surfactant functionalization; quaternized poly (vinyl alcohol); hydroxide-conduction; alkaline methanol fuel cell

1. Introduction

Global energy demands have become a major issue in the 21st century. Among the many energy resources, direct alcohol fuel cells (DAFCs) using polymer electrolyte membranes are some of the most promising energy sources. DAFCs have a simple liquid fuel system, high power/energy densities, high energy efficiency, and low cost for stationary, automotive and portable devices in small-to-large scale applications [1,2]. DAFCs may be operated in two modes: acidic and alkaline types. The acidic mode employs proton-exchange (H$^+$) polymer electrolytes, while the alkaline mode uses hydroxide ion (OH$^-$) conductive membranes. The advantages of using hydroxide-conducting membranes include

the feasibility of using non-precious metal catalysts, reduced fuel crossover, inexpensive components, and low cost [3,4]. In addition, the kinetics of methanol oxidation are faster in alkaline solutions than in acidic media, which produces improved electrode kinetic reactions [2]. Moreover, the hydroxide anion transport path opposes the methanol flux to decrease methanol permeability and improve the cell performance [5,6]. Cell voltage and power densities using hydroxide-conducting DAFCs have shown promising results, with equivalent or even higher cell performance compared with proton exchange DAFCs [4,7–9].

Poly(vinyl alcohol) (PVA) has good film-forming property to assemble efficient electrolyte and good stability after doping with a potassium hydroxide (KOH) solution [6,10]. This PVA membrane separator has been well established for various alkaline batteries and fuel cells [11–13]. The integrity of PVA material in alkaline solution and redox environment has been confirmed [14–16]. After being functionalized with ammonium groups, quaternized PVA (QPVA) membranes demonstrated high alkaline fuel cell performance and stable energy output for at least 280 h for direct alkaline methanol fuel cells (DAMFCs) [17,18].
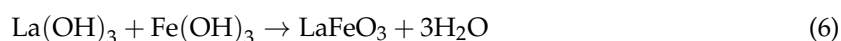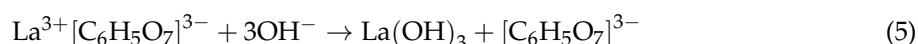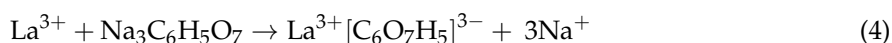
Incorporating organic/inorganic nanofillers (e.g., chitosan, Al_2O_3, SiO_2, TiO_2, and Fe_3O_4) into a PVA-based matrix has been shown to enhance chemical stability, physicochemical, and electrochemical properties for DAMFC applications [17,19–22]. These nanocomposite membranes deliver noteworthy advantages over traditional pure polymeric membranes due to their higher ionic conductivity, suppressed permeability, and improved power densities [23,24]. Among the different nanofillers, perovskite-type oxides (with a chemical structure of ABO_3) have recently attracted much attention in energy-based and conversion applications such as solar cells, photocatalysis, electrode catalysis, lithium-ion batteries, supercapacitors, and fuel cells [25,26]. Perovskite-based $LaFeO_3$ nanofillers are potential anode materials to enhance methanol oxidation rates [27,28]. Among various wet chemical methods involved in the growth of $LaFeO_3$ nanoparticles [29], a surfactant-assisted hydrothermal process has significant advantages [30]. These advantages include high phase purity, chemical stability, large surface areas, monodispersed shape/size, low temperature growth, oxygen non-stoichiometric qualities, and cost-effectiveness over the above-mentioned spinel metal oxide nanofillers [31–33]. In addition, defects in ABO_3 generated from cation deficiencies in either A or B sites, or oxygen deficiency, can be easily manipulated by partial substitutions that exhibit high proton or oxygen ion conductivity [30,34]. Unemoto et al. reported that the conductivity of the perovskite oxide increased due to the variation of oxygen non-stoichiometry, accompanied by partial reduction of Fe ions in the perovskite oxide [35]. Recently, Cordero et al. reported theoretical and experimental investigations of the diffusion of oxygen vacancies and ionic mobilities of perovskite oxides for generating fast ion conduction in fuel cells [36]. Therefore, non-stoichiometry perovskite oxides could enable high ionic conductivity due to strong interactions between oxygen vacancies [37].

In making an effective membrane electrolyte, the interfaces between the nanofillers and the polymer matrix play a critical role. Several adverse phenomena, such as void formation and polymer chain rigidification at the interfaces of the fillers and polymer matrix, can result in unexpected outcomes of transport properties of small molecules through the composite membrane. In the current work, $LaFeO_3$ nanoparticles are used as nanofillers for the electrolyte membrane in DAMFCs for the first time. Herein, we report on the preparation of perovskite $LaFeO_3$ nanoparticles via a hydrothermal process with cetyltrimethylammonium bromide (CTAB) as a surfactant agent. Surfactant-coated $LaFeO_3$ nanoparticles were prepared in the synthesis procedure. Annealed, crystalline $LaFeO_3$ nanoparticles without surfactant were also prepared. Both perovskite $LaFeO_3$ nanofillers were incorporated into a QPVA matrix and cast into thin films. The resulting composites were characterized and tested for their alkaline fuel cell performance. The possible interactions from incorporating 0.1 wt % $LaFeO_3$ nanoparticles into the QPVA matrix and the surfactant role on the film formation and transport mechanism are elucidated. To the best of our knowledge, the current work provides an introductory report on the preparation of a QPVA/$LaFeO_3$ nanocomposite membrane for use as an alkaline hydroxide-conducting membrane for DAMFCs.

2. Results and Discussion

### 2.1. Perovskite Reaction Mechanism and Morphological Analysis

The amorphous $LaFeO_3$ nanoparticles were prepared using a simple hydrothermal method. The reaction time and temperature of this hydrothermal reaction resulted in enhanced formation of nanosized particles coated with a cationic surfactant. Distilled (D.I.) water permits the suspension of highly polar organic and inorganic compounds, which makes it a highly viscous and effective medium. Additionally, this process slows the diffusion of metal ions and assists in the formation of new nuclei to induce the growth of nanoparticles [38]. The possible chemical reaction of the $LaFeO_3$ nanoparticles can be proposed as follows:

$$La(NO_3)_3 \rightarrow La^{3+} + 3NO_3^- \tag{1}$$

$$Fe(NO_3)_3 \rightarrow Fe^{3+} + 3NO_3^- \tag{2}$$

$$Fe^{3+} + 3OH^- \rightarrow Fe(OH)_3 \tag{3}$$

$$La^{3+} + Na_3C_6H_5O_7 \rightarrow La^{3+}[C_6O_7H_5]^{3-} + 3Na^+ \tag{4}$$

$$La^{3+}[C_6H_5O_7]^{3-} + 3OH^- \rightarrow La(OH)_3 + [C_6H_5O_7]^{3-} \tag{5}$$

$$La(OH)_3 + Fe(OH)_3 \rightarrow LaFeO_3 + 3H_2O \tag{6}$$

Initially, the $La(NO_3)_3$ was dissolved in D.I. water to produce La^{3+} ions (Equation (1)) with continuous stirring under ambient conditions. Similarly, Fe^{3+} ions were generated when $Fe(NO_3)_3$ was mixed in D.I. water in the same atmosphere (Equation (2)). The generated Fe^{3+} ions were further hydrolysed to form $Fe(OH)_3$ under hydrothermal temperatures (Equation (3)). The La^{3+} ions coalesced more simply with trisodium citrate via chelating effects (Equation (4)). Furthermore, La^{3+} ions are slowly released and gradually transformed into $La(OH)_3$ via a hydrolysis reaction (Equation (5)). At the same time, $Fe(OH)_3$ reacts with $La(OH)_3$ at higher temperatures to produce the amorphous phase of the $LaFeO_3$ nanoparticles via a condensation process (Equation (6)). In addition, the CTAB molecules play an essential role in tuning the size and shape of the $LaFeO_3$ nanoparticles via growth units and aggregation effects.

Systematic investigation was performed to understand the structure of the perovskite $LaFeO_3$ nanoparticles with varying annealing temperatures. The transmission electron microscope (TEM) images of the CTAB-coated $LaFeO_3$ nanoparticles and those annealed at 800 °C were analysed, as shown in Figure 1a,b. The TEM images in Figure 1a shows non-uniformly shaped core particles with a size of ~50 nm and CTAB-coated particle surfaces. The arrangement of the smaller core particles occurs due to the slow diffusion process of homogeneous nucleation via the effect of the surfactant. The CTAB surfactant molecules can attach onto specific crystal facets, which makes it possible to control the size and shape of the final crystal structure and prevent particle aggregation [39]. The CTAB coating was further confirmed by high-resolution TEM (HRTEM) imaging as observed in Figure 1b. Liu et al. [40] have reported that electrostatic interaction between the hydrocarbon group of CTAB and perovskite nanoparticles improves the surfactant coating and increases particle stability. We hypothesized that the cationic surfactant molecules would strongly coat nanoparticles via self-assembly to enhance the surface properties [41,42]. The $LaFeO_3$ nanoparticles were annealed at different temperatures, as shown in supplementary Figure S1a–c. When the temperature was raised to 800 °C, the tightly arranged primary particles were compressed to form spherically shaped crystalline nanocrystals, as shown in Figure 1c,d. The Ostwald ripening process plays an active role to produce a spherical shape via the trapping of smaller particles [43]. At 800 °C, the cationic surfactant was completely removed from the particle surface and high crystallinity particles were confirmed, as shown in the HRTEM image (Figure 1d) and XRD pattern (Figure 2a). Therefore, different annealing temperatures have significant effects on the surfactant functionalization and the crystallinity of the resulting $LaFeO_3$ nanoparticles.

The energy dispersive X-ray (EDX) spectroscopy results of the CTAB-coated $LaFeO_3$ nanoparticles and those annealed at 800 °C are shown in supplementary Figure S2a,b.
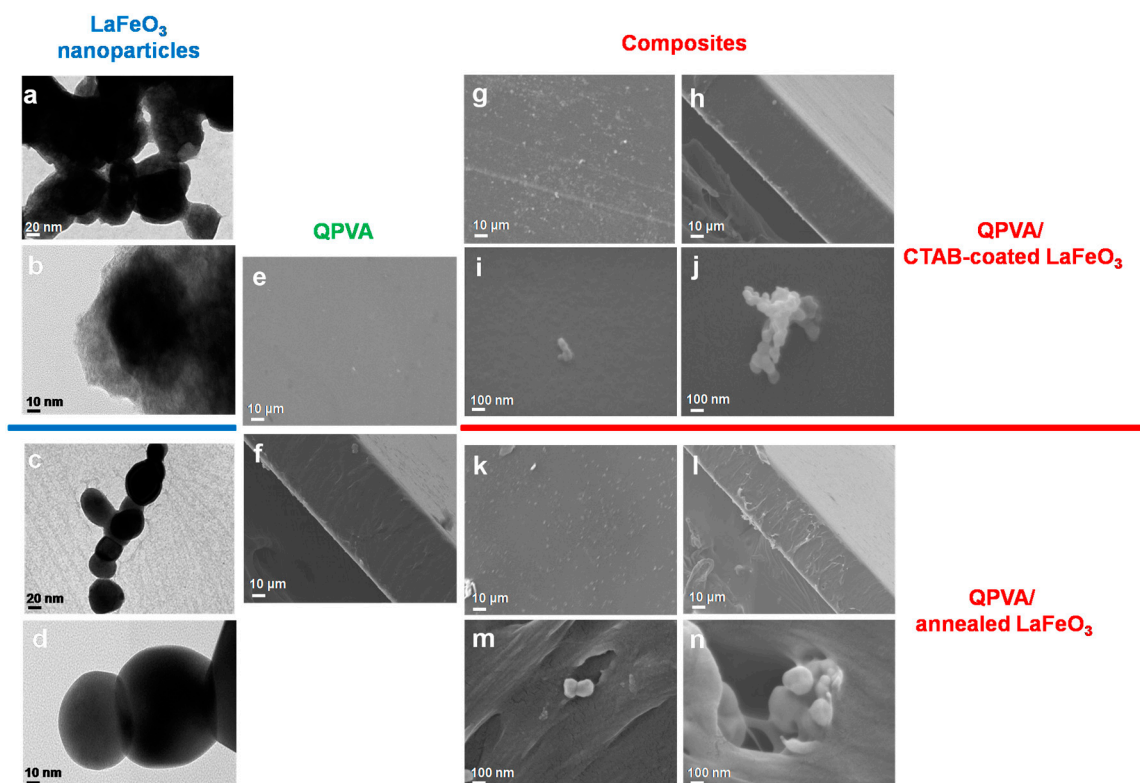
Figure 1. Transmission electron microscope (TEM) and high-resolution TEM (HRTEM) images of $LaFeO_3$ nanoparticles of: (**a**,**b**) cetyltrimethylammonium bromide (CTAB)-coated; (**c**,**d**) 800 °C annealed samples, and field emission scanning electron microscope (FESEM) surface and cross-sectional morphology of: (**e**,**f**) quaternized poly(vinyl alcohol) (QPVA) membrane; (**g**–**j**) QPVA/CTAB-coated $LaFeO_3$; and (**k**–**n**) QPVA/annealed $LaFeO_3$ nanocomposite membrane.

2.2. Physicochemical Characterization of Nanoparticles

The crystal structure of the $LaFeO_3$ nanoparticles was analysed using X-ray diffraction (XRD) as shown in Figure 2a. The XRD pattern of the CTAB-coated $LaFeO_3$ nanoparticles showed an amorphous phase, as did those annealed at 200 °C and 400 °C. With increasing temperature to 600 °C, the amorphous $LaFeO_3$ nanoparticles transformed into the single-phase orthorhombic crystalline structure of perovskite $LaFeO_3$ (Figure 2a) [44,45]. When the temperature was raised to 800 °C, a good crystalline phase was observed with high intensity. All of the diffraction peaks matched to the orthorhombic structure and were indexed with bulk $LaFeO_3$ crystals (JCPDS:37-1493) [46]. No other impurities (including characteristic peaks of metal nitrate, Fe_2O_3 or La_2O_3) were observed [47]. Scherrer's formula was employed to calculate the average grain size, which was approximately 23 nm for the 800 °C-annealed $LaFeO_3$ nanoparticles. Based on X-ray photoelectron spectroscopy (XPS) data, we found out that the actual structure of the prepared perovskite nanoparticles was probably $La_{0.8}FeO_{2.7}$. Similar perovskite structure was also reported by Spinicci et al. using low temperature thermal decomposition method [32]. The oxygen non-stoichiometry effect was common when the nanoparticles were prepared using auto-combustion, thermal-decomposition, citrate pyrolysis, solid state reaction and Pechini methods [32,47–49]. Delmastro et al. [50] showed that a series of these perovskite structures (including $LaFeO_3$ and $La_{0.7}FeO_{2.55}$) demonstrated identical XRD patterns. Therefore, we used the term of $LaFeO_3$ to present actual perovskite nanostructure in this manuscript.
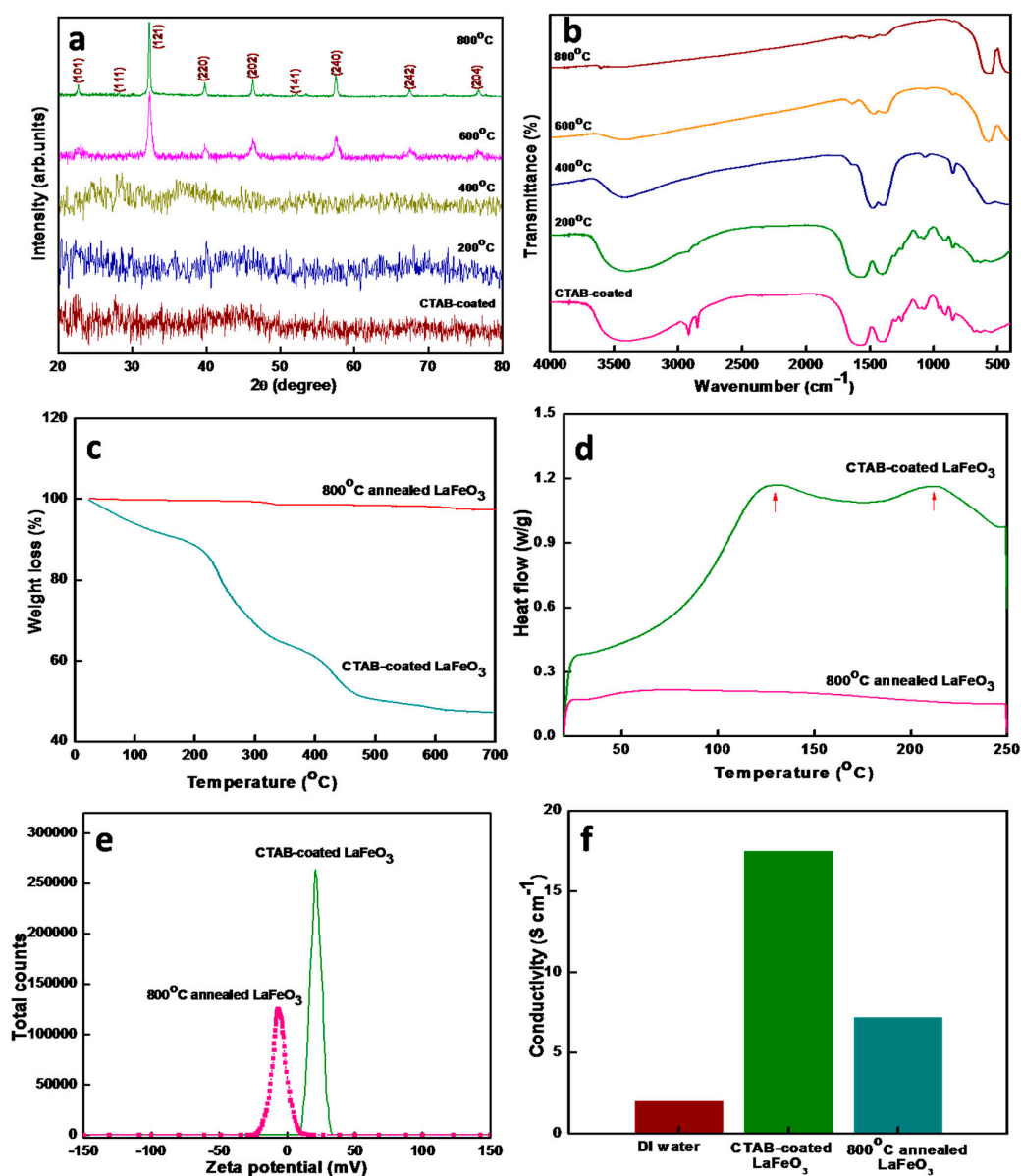
Figure 2. (**a**) X-ray diffraction (XRD) patterns; and (**b**) Fourier transform infrared spectroscopy (FTIR) spectra of CTAB-coated LaFeO$_3$ nanoparticles and those annealed at various temperatures; (**c**) thermo-gravimetric analysis (TGA) thermographs; (**d**) differential scanning calorimetry (DSC) thermographs; (**e**) zeta potential plot; and (**f**) conductivity of CTAB-coated and 800 °C annealed LaFeO$_3$ nanoparticles. Plots (**e**,**f**) are measured on nanoparticles in distilled water suspensions.

The functional group changes before and after LaFeO$_3$ nanoparticle annealing were analysed using the FTIR spectrum, as shown in Figure 2b. For CTAB-coated LaFeO$_3$ nanoparticles, the weak intensity band at 460 cm^{-1} confirms the formation of a metal oxide phase. This peak was slightly shifted to a lower wavenumber compared with the values reported in the literature, which might be due to the amorphous phase of the LaFeO$_3$ nanoparticles [46]. The small, intense peaks at 910 cm^{-1}, 1096 cm^{-1}, and 1238 cm^{-1} represent –N–H– bending and –C–N–stretching vibrations due to the presence of nitro compounds. The strong peaks at 1568 cm^{-1} and 1417 cm^{-1} were attributed to C–H scissoring vibrations of the –N–CH$_3$ moiety corresponding to CTAB molecules, which confirms the presence of the surfactant [25]. The two weak bands at approximately 2920 cm^{-1} and 2858 cm^{-1} represent asymmetric and symmetric stretching vibrations of –CH$_2$ molecules. Another broad absorption peak

from N–H stretching vibrations of the amino group was located at approximately 3405 cm^{-1}; it might overlap with the vibration bands associated with –OH groups. When the annealing temperature was raised to 400 °C, peak intensity at 552 cm^{-1} began to increase, indicating that the metal oxide bonding was strengthened due to the initial growth of the crystalline phase from the amorphous nanoparticles. The corresponding peak intensity of the CTAB molecules decreased and slightly shifted to a lower wavenumber (~30 cm^{-1}) due to decomposition of the CTAB molecules. On further increasing the temperature to 600 °C and 800 °C, no characteristic CTAB peaks were observed. The broad and strong spectroscopic band at 562 cm^{-1} corresponds to the symmetric Fe-O stretching vibration of the octahedral FeO_6 in $LaFeO_3$ and indicates the formation of a perovskite structure [46]. The results confirm that the CTAB-coated $LaFeO_3$ nanoparticles display ammonium functional groups via the presence of the surfactant, whereas the annealed nanoparticles do not exhibit noteworthy associated functional groups.

The thermal stability of the CTAB-coated and 800 °C-annealed $LaFeO_3$ nanoparticles was observed via TGA analysis, as shown in Figure 2c. Minimal weight loss (2–3%) was observed for the annealed sample whereas three distinct weight losses were obtained for CTAB-coated $LaFeO_3$ nanoparticles. Below 200 °C, the CTAB-coated $LaFeO_3$ underwent an 11% weight loss due to the elimination of surface-adsorbed water molecules or hydroxyl groups. The second weight loss, from 200 °C to 320 °C, occurred due to the desorption and decomposition of molecular organic residuals of the surfactants, such as C–N, C=O and C–H. The third weight loss, up to 460 °C, was due to the decomposition of nitrate molecules. No further weight loss was observed after ~500 °C [38].
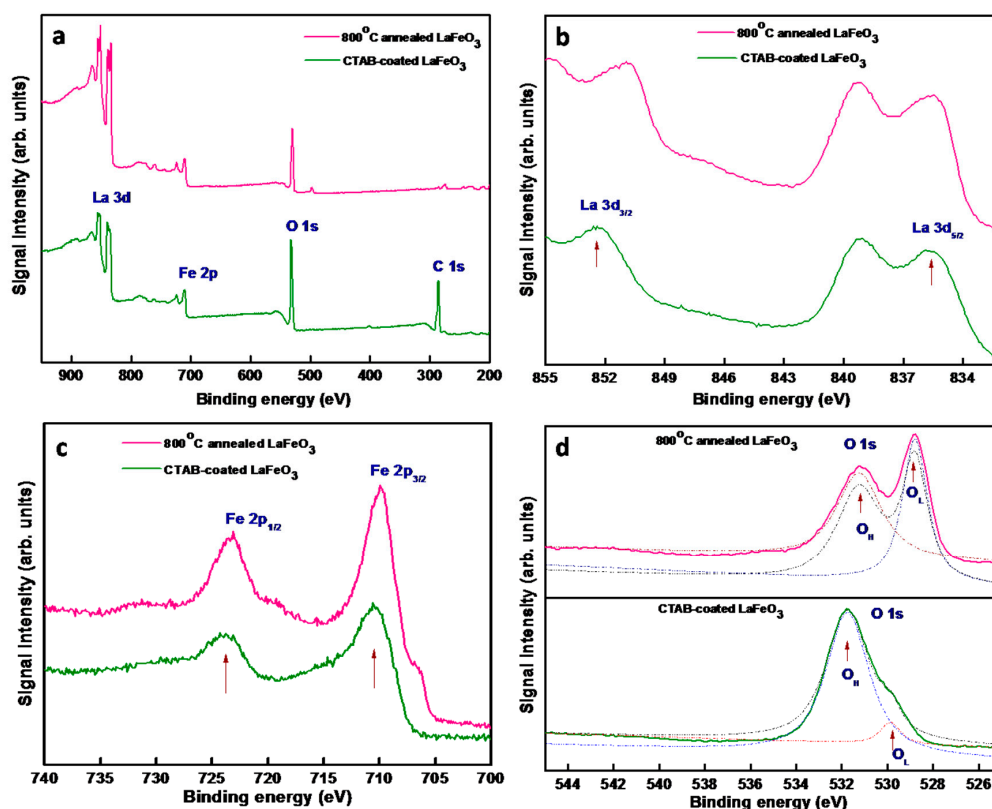
The CTAB-coated $LaFeO_3$ nanoparticles and those annealed at 800 °C were characterized using differential scanning calorimetry (DSC), and the results are shown in Figure 2d. The CTAB-coated $LaFeO_3$ nanoparticles show two distinct exothermic peaks at 128 °C and 212 °C. The first exothermic peak was attributed to the loss of lattice water, whereas the elimination or degradation of organic residuals from the CTAB molecules accounts for the second exothermic peak. In the case of the annealed $LaFeO_3$ nanoparticles, no apparent mass loss was observed (Figure 2c), which confirms the absence of functional molecules and establishes the thermal stability.

The cationic surfactant CTAB may affect the surface charge of the $LaFeO_3$ nanoparticles; its zeta potential is shown in Figure 2e. The annealed $LaFeO_3$ nanoparticles had a negative surface charge of −4.9 mV. The CTAB-coated $LaFeO_3$ nanoparticles had a positive surface charge of +20.7 mV, implying that ammonium groups were at the outermost layer of the CTAB-functionalized nanoparticles. The solution conductivity of the nanoparticles suspension was examined to further confirm the surface charge effect (Figure 2f). Distilled water was used as a solvent for dispersing the $LaFeO_3$ nanoparticles. The ionic conductivity of the pure distilled water was 2.0×10^{-6} S cm^{-1}. The annealed $LaFeO_3$ nanoparticles suspension had an ionic conductivity of 7.2×10^{-6} S cm^{-1}. The CTAB-coated $LaFeO_3$ nanoparticles suspension showed a significantly higher ionic conductivity of 17.5×10^{-6} S cm^{-1}. The CTAB-coated $LaFeO_3$ nanoparticles had a higher conductivity than that of the annealed nanoparticles due to higher surface charge.

2.3. Compositional Analysis of Nanoparticles

The elemental composition and electronic state of the CTAB-coated $LaFeO_3$ nanoparticles and those annealed at 800 °C were studied via XPS. Figure 3a shows that the surfaces of both CTAB-coated $LaFeO_3$ nanoparticles and those annealed at 800 °C contained four different elements (La, Fe, O and a trace amount of C) without other impurities. The Fe 2p and La 3d core-level orbit spectra showed that the iron and lanthanum atoms were in the +3 chemical valence state. Figure 3b shows the La 3d core level at 852.3–835.6 eV, confirming the presence of La 3d$_{5/2}$ and La 3d$_{3/2}$. The satellite peak with a higher binding energy at 839.1 eV matched with La 3d$_{5/2}$, demonstrating a core hole with an electron transferred from the O 2p valence band to an empty La 4f orbital [51]. In Figure 3c, the XPS signals at 709.9 eV and 723.5 eV represent the Fe 2p$_{3/2}$ and Fe 2p$_{1/2}$ orbits, respectively, values ascribable to the Fe^{3+} ionic surfaces due to spin-orbital splitting form. The deconvolution of the O 1s peak

revealed two oxygen chemical states at 528.9 and 531.7 eV, corresponding to O_L and O_H, respectively. The CTAB-coated LaFeO$_3$ showed a significant peak at 531.3 eV, attributable to chemisorbed water species to the hydroxyl groups associated with the surface of lanthanum oxide [52]. The CTAB-coated LaFeO$_3$ had a stronger ability to form active oxygen hydroxyl (O_H) adspecies. The annealed LaFeO$_3$ had a strong peak (528.8 eV), originating from La-O and Fe-O bonds via crystal lattice oxygen (O_L). The other strong peak of the annealed LaFeO$_3$ nanoparticles, at 531.7 eV, was recognized to correspond to hydroxyl oxygen (O_H) adsorbed on the nanoparticles surface resulting from the chemisorbed water [26].

Figure 3. (**a**) X-ray photoelectron spectroscopy (XPS) full spectra; (**b**) La 3d; (**c**) Fe 2p; and (**d**) O 1s spectra of CTAB-coated and 800 °C annealed LaFeO$_3$ nanoparticles.

2.4. Nanocomposite Membrane Characterizations

An FESEM was used to analyse the surface and cross-sectional morphology of the membranes. The surfaces of the QPVA, QPVA/CTAB-coated LaFeO$_3$, QPVA/annealed LaFeO$_3$ composites were flat and smooth, confirming the formation of dense membranes (Figure 1e,g,k). The corresponding cross-section of the QPVA/CTAB-coated LaFeO$_3$ (Figure 1h,j) and QPVA/annealed LaFeO$_3$ (Figure 1l,n) membranes displayed nanofiller distribution in the polymeric film. The nanoparticles may form primary particles or aggregates of up to tens of primary particles (Figure 1i,j,m,n). It was noted that the QPVA/annealed LaFeO$_3$ membrane had interfacial defects (Figure 1m,n), whereas the QPVA/CTAB-coated LaFeO$_3$ film was pinhole-free. The rigid crystalline LaFeO$_3$ nanoparticles were not compatible with the soft QPVA segments, and voids formed during the film drying process. In contrast, the CTAB served as an intermediate medium, bridging the LaFeO$_3$ nanoparticles and QPVA chains, and resulted in a defect-free structure (Figure 1i,j).

EDX was used to analyse the elemental mapping and composition of the nanocomposite membranes. The presence of elemental C (55.26 wt %), O (43.16 wt %), La (0.53) and Fe (1.05 wt %) in the QPVA/CTAB-coated LaFeO$_3$ nanocomposite membrane can be seen in Figure S3a. Similarly, the

QPVA/annealed LaFeO$_3$ nanocomposite membrane (Figure S3b) also reveals the presence of La, Fe and O elements.

The phase purity and crystallinity of the QPVA/CTAB-coated LaFeO$_3$ and QPVA/annealed LaFeO$_3$ membranes were analysed using XRD analysis, as shown in Figure 4a. The QPVA membrane had a quarterisation efficiency of 3–4% [10], and the other 96–97% of the polymeric matrix retained the PVA structure [53–55]. Therefore, the QPVA nanocomposite membranes showed a semi-crystalline structure with an XRD peak at 2θ of 20°, corresponding to the (101) plane of the PVA crystal structure [17,53–55]. The nanocomposite membrane intensity decreased compared with pristine PVA, as described in our previous study [53], yet the QPVA composites retained good film structure [17,18,23]. This result implies that the addition of nanofiller to the polymeric matrix greatly suppressed the crystalline domains [18,23].
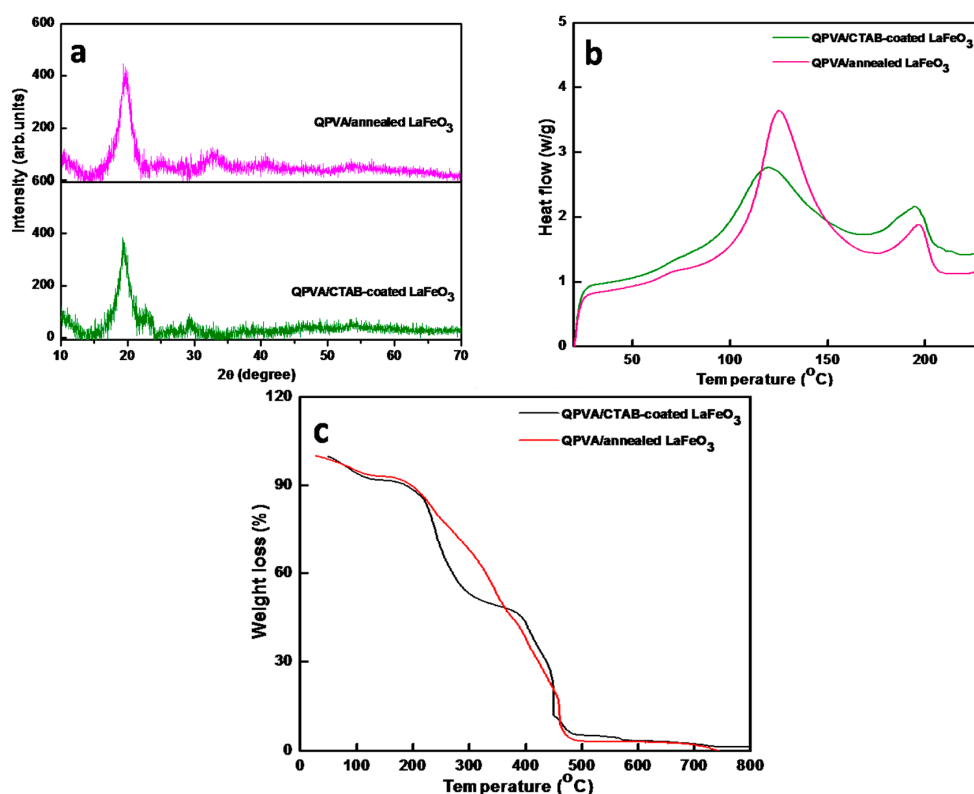
Figure 4. (**a**) XRD patterns; (**b**) DSC thermographs; and (**c**) TGA thermographs of QPVA/CTAB-coated LaFeO$_3$ and QPVA/annealed LaFeO$_3$ nanocomposites.

To further evaluate the polymer crystallinity of the nanocomposite membrane, DSC thermographs were used to measure the melting enthalpies. The DSC thermographs of the QPVA/CTAB-coated LaFeO$_3$ and QPVA/annealed LaFeO$_3$ membranes are shown in Figure 4b. The QPVA/CTAB-coated LaFeO$_3$ shows an exothermic peak at 120 °C that corresponds to the removal of water molecules or the degradation of organic residuals. The second exothermic peak, at 195 °C, is associated with degree of polymer crystallinity. The crystallinities of the QPVA/CTAB-coated LaFeO$_3$ and QPVA/annealed LaFeO$_3$ membranes were calculated [55] to be 26.45% and 30.80%, respectively. The crystallinity of the QPVA/CTAB-coated LaFeO$_3$ membrane decreased due to the strong interaction between the CTAB surfactant and the QPVA polymer chains, which caused interruption of the polymer chain alignment. This result illustrates that the polymeric amorphous state was 69.2% for the QPVA/annealed LaFeO$_3$ membrane and 73.55% with the QPVA/CTAB-coated LaFeO$_3$ nanocomposite. Increasing the amorphous region could improve the ionic conductivity and cell performance of DAMFCs [20,56].

Figure 4c shows the TGA curves of the QPVA, QPVA/CTAB-coated $LaFeO_3$, and QPVA/annealed $LaFeO_3$ nanocomposite membranes. The initial weight loss of the QPVA/CTAB-coated $LaFeO_3$ membrane was observed at 210 °C due to the evaporation of water or hydroxyl molecules. The second weight loss (~35–40%) was observed at 210–340 °C due to the decomposition of the ammonium groups or residual functional groups from a surfactant. The third weight loss occurred via degradation of the QPVA polymer main chain and side chain molecules due to thermal cracking at temperatures above 350 °C [2]. Thus, the thermal stability of the QPVA/CTAB-coated $LaFeO_3$ membrane was improved, in comparison to that of the QPVA/annealed $LaFeO_3$, due to strong binding of the surfactant-coated nanofillers in the polymer matrix.

Young's modulus and elongation at break values are shown in Table 1. The elongation of pristine QPVA is 143% due to the flexibility of the membrane, which relies on PVA content [57]. In the case of the nanocomposite membranes, flexibility decreases to 99% or 54% with the addition of 0.1% CTAB-coated or annealed $LaFeO_3$ nanofillers in the membrane matrix, respectively. Moreover, the Young's modulus values of the QPVA/CTAB-coated $LaFeO_3$ and QPVA/annealed $LaFeO_3$ nanocomposite membrane decreased due to decreasing crystallinity of the QPVA polymer chains. Therefore, nanocomposite membrane's mechanical stability was sacrificed by the addition of $LaFeO_3$ nanofillers. However, the composite with CTAB-coated nanofillers demonstrated less mechanical strength loss than that containing annealed $LaFeO_3$ due to better interfacial compatibility between the polymer and nanofillers.

Table 1. Mechanical strength, ion-exchange capacity, total KOH uptake, and swelling ratio of pristine QPVA, QPVA/0.1%CTAB-coated $LaFeO_3$, and QPVA/0.1% annealed $LaFeO_3$ nanocomposite membranes.

Properties	QPVA	QPVA/CTAB-Coated $LaFeO_3$	QPVA/Annealed $LaFeO_3$
Elongation (%)	143	99	54
Young's modulus (MPa)	22.3	12.3	6.9
Ion exchange capacity (mmol g^{-1})	0.75 ± 0.02	1.06 ± 0.04	0.95 ± 0.01
Total KOH solution Uptake (g g^{-1}) [a]	2.14 ± 0.01	1.43 ± 0.02	1.30 ± 0.01
Partial KOH uptake (g g^{-1}) [a]	0.48	0.78	0.58
Partial water uptake (g g^{-1}) [a]	1.66	0.65	0.72
In-plane swelling (%) [a]	25.0	6.3	10.0
Through-plane swelling (%) [a]	66.7	44.4	51.1

[a] Measured after immersing the membranes in 6 M KOH solution at 30 °C.

Methanol permeability values of the pristine QPVA, QPVA/CTAB-coated $LaFeO_3$ and QPVA/annealed $LaFeO_3$ nanocomposite membranes are shown in Figure 5a. The permeability of the pristine QPVA membrane was 5.08×10^{-6} cm^2 s^{-1} at 30 °C using 6 M KOH and 2 M methanol as a source reservoir. However, permeability was suppressed to 3.10×10^{-6} cm^2 s^{-1} (a 39% decrease) and 3.50×10^{-6} cm^2 s^{-1} (a 31% decrease) for the QPVA/CTAB-coated $LaFeO_3$ and QPVA/annealed $LaFeO_3$ membranes, respectively. The incorporation of the nanofillers in the QPVA film resulted in physical hindrance, blocking the passage of fuel feed and reducing the alcohol crossover [58,59]. This effect is advantageous for the polymeric electrolyte membrane in improving cell performance of DAMFCs [60].

To evaluate the stability of the nanocomposite membrane, dissolution in water was studied [55]. The dissolution values of KOH-doped QPVA and nanocomposite membranes are shown in supplementary Figure S4. Approximately 24.7% of the QPVA membrane dissolved in water at 25 °C during 72 h of immersion. However, the dissolution values of QPVA/CTAB-coated $LaFeO_3$ (10.23%) and QPVA/annealed $LaFeO_3$ (12.59%) were significantly lower. Incorporating 0.1% of $LaFeO_3$ nanofillers in the polymeric matrix prevented the polymer chain from unfolding, which resulted in lower water solubility. We have found similar results for PVA/fumed silica nanocomposites [53]. The improved stability is likely attributable to the physical cross-linking between the nanofillers and polymer chains [55].
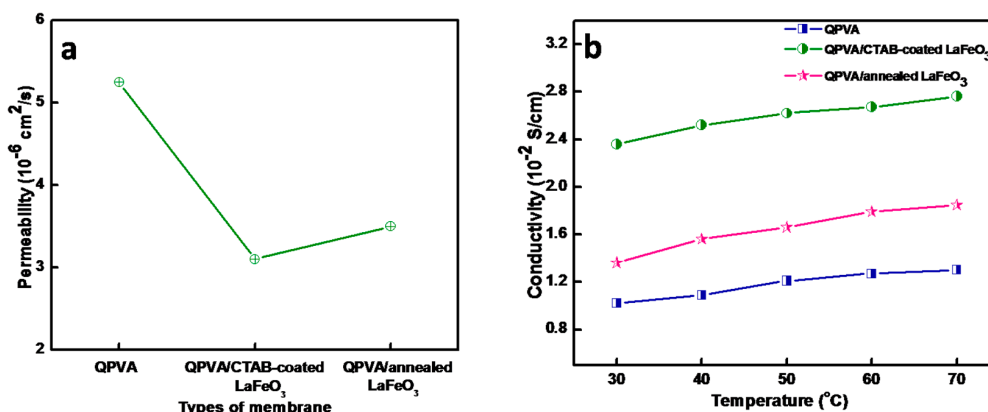
Figure 5. (**a**) Methanol permeabilities of QPVA, QPVA/CTAB-coated LaFeO$_3$, and QPVA/annealed LaFeO$_3$ nanocomposite membrane at 30 °C; and (**b**) ionic conductivities of QPVA, QPVA/CTAB-coated LaFeO$_3$, and QPVA/annealed LaFeO$_3$ nanocomposites operated at 30–70 °C.

The ionic exchange capacities (IEC) of the pristine and nanocomposite membranes are shown in Table 1. The QPVA/CTAB-coated LaFeO$_3$ membrane showed a higher IEC (1.06 mmol g^{-1}) than the pristine QPVA membrane (0.752 mmol g^{-1}). Hong et al. [61] have proposed that loading low percentages of nanofillers into the membrane leads to higher IEC values due to strong interactions between the nanofillers and polymers. The higher IEC values in the nanocomposite membranes are in line with partial KOH uptakes, observed to be higher than that of the pristine QPVA film (as explained below).

The total KOH solution uptake was 2.14 g g^{-1} for QPVA, whereas it was 1.43 g g^{-1} and 1.30 g g^{-1} for the QPVA/CTAB-coated LaFeO$_3$ and QPVA/annealed LaFeO$_3$ membranes. This quantity can be divided into two parts: the mass uptake due to KOH and the mass uptake due to water adsorption. Although QPVA had a higher total KOH solution uptake than that of the other two nanocomposites, the majority (~78%) of the uptake was due to water sorption. In contrast, the nanocomposite membranes exhibited higher partial KOH uptake (0.78–0.58 g g^{-1}) and lower partial water uptake (0.65–0.72 g g^{-1}) than those of the pristine QPVA membrane (Table 1). This increased KOH uptake in the nanocomposite membranes may be due to their higher IEC values and reduced polymer crystallinity in the QPVA matrix [62].

The higher partial water uptake in the pristine QPVA membrane was associated with a higher swelling ratio than that of the nanocomposite membranes (Table 1). The adsorbed water molecules tended to swell the films, and the membrane volumes increased. However, the swelling was not isotropic; the thickness along the through-plane direction increased 2–7-fold higher than that of the width and length (Table 1). The smaller swelling ratio of the nanocomposite membranes enhanced their dimensional stability (especially in the through-plane direction). It was beneficial for maintaining good interfacial contacts between the membrane and the electrodes, thus improving single cell conductivity.

Ionic conductivities of the QPVA, QPVA/CTAB-coated LaFeO$_3$, and QPVA/annealed LaFeO$_3$ membranes as a function of temperature are shown in Figure 5b. The ionic conductivities of the pristine QPVA ranged from 1.02×10^{-2} to 1.30×10^{-2} S cm^{-1} at 30–70 °C. The results confirm that conductivity gradually increased with increasing temperature; the hydroxyl ions/molecules diffuse more easily due to thermal activation processes [2]. The ionic conductivity of the QPVA/CTAB-coated LaFeO$_3$ membrane gradually increased from 2.36×10^{-2} to 2.76×10^{-2} S cm^{-1} at the same temperatures. The conductivity of the nanocomposite membrane increased to double than that of the pure QPVA membrane. The oxygen non-stoichiometric effects of LaFeO$_3$ nanofiller may results from ionic configuration on the Fe cation and transport of OH$^-$ ions via oxygen vacancies that enhance the conductivity [29,37]. In the case of the QPVA/annealed LaFeO$_3$ nanocomposite membrane, the ionic conductivity was slightly lower (1.36×10^{-2}–1.85×10^{-2} S cm^{-1}) than that of the QPVA/CTAB-coated

LaFeO$_3$, but higher than that of the QPVA membrane. Decreased KOH uptake of the QPVA/annealed LaFeO$_3$ membrane reduces ionic conductivity due to shrinkage of the effective hydroxyl diffusion channels. The results clearly demonstrate that the incorporation of CTAB-coated LaFeO$_3$ nanoparticles in the QPVA matrix enhances conductivity, probably due to defect-free interfacial adhesion between polymer and fillers.

The hydroxide conductivity of the KOH-doped QPVA nanocomposite membranes was higher than that of most alkaline anionic exchange membranes (which are of the order of 10^{-2}–10^{-3} S cm^{-1} [2,7,21,23,63]). The quaternized portion acted as an anionic-exchange membrane, and its conductivity was comparable to that of most anion-exchange membranes [18,21]. The higher ionic conductivity was due to a hopping mechanism at the anionic-exchange functional group and to the vehicular diffusion through the polymeric free volume in the QPVA matrix [17].

An Arrhenius-type relationship was recognized for the three types of electrolyte membranes' dependence on temperature effects. The activation energy of the pristine QPVA membrane was 20.11 kJ mol^{-1}. Activation energies decreased to 16.04 kJ mol^{-1} and 7.98 kJ mol^{-1} for the QPVA/annealed LaFeO$_3$ and QPVA/CTAB-coated LaFeO$_3$ nanocomposite membranes, respectively. The different mechanisms of ionic transfer phenomena in the nanocomposite membranes are responsible for the different activation energies.

2.5. Role of CTAB Surfactant

Most researchers have used crystalline LaFeO$_3$ nanoparticles toward potential applications, but data comparison with respect to amorphous LaFeO$_3$ nanoparticles is limited [46,64–66]. To elucidate the effects of surfactant (CTAB) and LaFeO$_3$ nanofillers (amorphous vs. crystalline), different fillers were added into PVA matrix (which is the major dominant constituent of the QPVA) to form composites, and their conductivities were measured at 30–60 °C. The fillers included pure CTAB, pure LaFeO$_3$ nanofillers (amorphous phase without CTAB), as-synthesized LaFeO$_3$ nanofillers (CTAB-functionalized amorphous phase), and annealed LaFeO$_3$ nanofillers (crystalline). Since the as-synthesized LaFeO$_3$ nanofillers contain almost 50% CTAB and 50% perovskite by weight (Figure 2c), a half load of the individual additive component (CTAB and LaFeO$_3$) was incorporated into the PVA for fair comparison.

The PVA film had a conductivity value of 1.80–1.89 mS cm^{-1} at 30–60 °C (Table S3). As 0.05% CTAB was incorporated into the PVA, conductivity values increased by 66–102% at the same temperature range. This may be due to more ammonium functional groups from CTAB being introduced (in other words, to chemical factors) to the PVA. The addition of 0.05% of LaFeO$_3$ resulted in 119–149% increases of conductivity compared to unadulterated PVA. The increased polymer-free volume at the expense of polymer crystallinity due to nanofillers (in other words, physical factors, as shown in Figure 6a) may contribute to the enhanced ion transport and conductivity values. As more nanoparticles were added to the PVA, the same 0.1% load of amorphous or crystalline LaFeO$_3$ in the membrane did not render significantly different conductivity values (as shown in the last two rows in Table S3): both had 220–300% increases compared to the PVA sample. This implies that the nanoparticles improved the ionic conductivity due to physical factors; higher filler loads had more pronounced effects [53].

Now, if the PVA sample containing 0.1% CTAB-coated LaFeO$_3$ has similarly increased conductivity comparable to the combined conductivity increase values of 0.05% CTAB and 0.05% LaFeO$_3$ composites, an additive effect from both the chemical and physical factors is confirmed. However, our data indicated that the conductivities were much higher (380–510% increases as compared to PVA) than those for the composites containing individual additives, implying that the CTAB-coated LaFeO$_3$ demonstrate a synergistic effect.

CTAB is a cationic surfactant consisting of counterions, a hydrophobic tail group, and a hydrophilic head group with high attraction toward water molecules [67]. When CTAB was dispersed in ethylene glycol solvent (a polar solvent with a solubility parameter of δ_d = 29.1–33 J$^{1/2}$/cm$^{3/2}$), the tendency of solubility parameters led to a major micellisation contribution, as shown in Figure 6b [68,69]. The polar ammonium groups tended to form outer layers in the micelles to minimize

formation energy. Therefore, when $LaFeO_3$ nanoparticles were dispersed in this polar solvent, the non-polar hydrocarbon chain in the CTAB surrounded the $LaFeO_3$ nanoparticles (Figure 6c). As a result, positive surface charge was introduced compared to the CTAB-free $LaFeO_3$ samples, as shown in Figure 2e. Hence, more ammonium functional groups were present on the nanofiller surface (Figure 6c), which provided more anionic exchange function to enhance ionic conductivity.
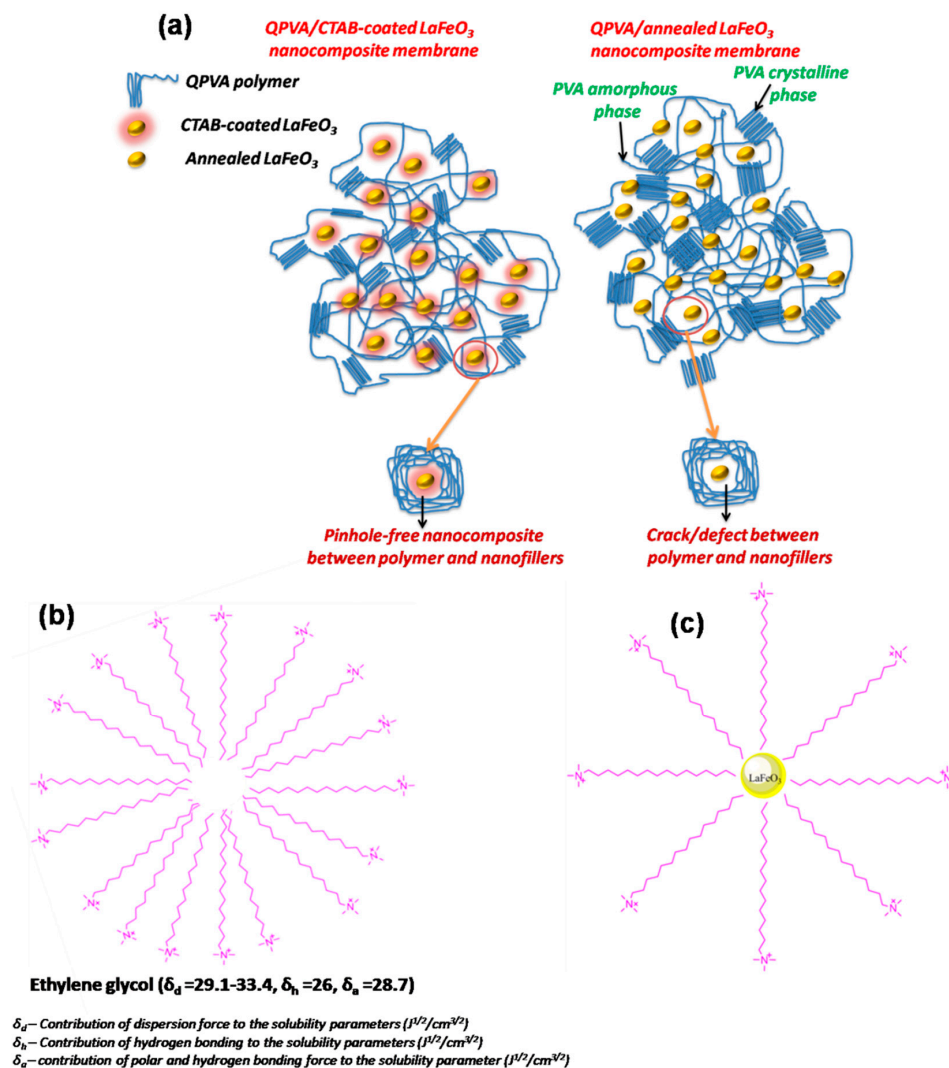
Figure 6. Schematic illustrations of: (**a**) the structures of QPVA/CTAB-coated $LaFeO_3$ and QPVA/annealed $LaFeO_3$ nanocomposite membranes; (**b**) CTAB micelle dispersed in polar ethylene glycol; and (**c**) interaction between CTAB molecules and $LaFeO_3$ nanoparticles.

The CTAB also serves as an intermediate binding layer between the $LaFeO_3$ particles and polymer chains on the membrane formation, as illustrated in the lower part of Figure 6a. Such a low-molecular-weight constituent forms a binder to link both particles and polymer chains for better interfacial compatibility. In other words, the CTAB might have played the role of plasticizer to fill in the defect between the rigid particles and the soft polymer matrix. Therefore, a pinhole-free composite was obtained (Figure 1i,j). Conversely, the annealed $LaFeO_3$ lacked this intermediate layer and cracks/defects resulted when the solvent evaporated and the film solidified. These cracks at the interfaces between particles and polymer region (Figure 1m,n) can lead to reduced transport properties, including a weaker gas barrier, and less film durability [70,71].

2.6. Direct Alkaline Methanol Fuel Cell Performance

To evaluate the reproducibility of the fuel cell performance, three replicate analyses were performed at 60 °C using 6 M KOH and 4 M methanol as the anode feed and the humidified oxygen (100 mL min^{-1}) in the cathode feed. The I–V plots of the QPVA/CTAB-coated LaFeO$_3$ and QPVA/annealed LaFeO$_3$ nanocomposite membranes are shown in supplementary information Figure S5a,b. The respective average cell potentials (V$_{OC}$) were found to be 0.653 V and 0.640 V with standard deviations of 0.009 and 0.008 V. The coefficients of variation of cell potential were 1.3% and 1.2%. The corresponding peak power density (P$_{max}$) is illustrated in supplementary information Figure S5c,d. The average values of P$_{max}$ were 108.33 and 95.66 mW cm^{-2} with experimental errors of 5.03 and 5.13 mW cm^{-2} and coefficients of variation of 4.6% and 5.3%, respectively. The V$_{OC}$ and P$_{max}$ of the QPVA/CTAB-coated LaFeO$_3$ and QPVA/annealed LaFeO$_3$ nanocomposite membranes show nearly equivalent experimental deviations (Tables S1 and S2), which demonstrates the good reproducibility of the performance measurements of DAMFCs.

The V$_{OC}$ and P$_{max}$ of DAMFCs with pristine QPVA electrolytes in 6 M KOH with various methanol concentrations (i.e., 1 M, 2 M, and 4 M) at 30 °C are shown in supplementary Figure S6. The 4 M methanol feed in the QPVA membrane produced higher fuel cell performance than did the 2 M and 1 M anode feeds at 30 and 60 °C. This result confirms that higher methanol concentration contributes to faster electro-kinetic reactions for enhanced P$_{max}$. In addition, more hydroxide ions are transferred via uptake of water/KOH in the QPVA membrane at a higher temperature and produce a higher P$_{max}$ (Table S2). The feasibility of using concentrated methanol feed into the DAMFCs with the QPVA electrolyte enables the generation of P$_{max}$ of one order of magnitude higher than other acidic [54] and alkaline methanol fuel cells [7,54,72] as reported in the literature.

The V$_{OC}$ and P$_{max}$ values for DAMFCs with different electrolytes using 4 M methanol in 6 M KOH at 30 °C are shown in Figure 7. The V$_{OC}$ of the QPVA membrane is 0.51 V, and the P$_{max}$ value is 71 mW cm^{-2}. Incorporating 0.1% CTAB-coated LaFeO$_3$ nanofillers into the QPVA matrix enhanced the V$_{OC}$ and P$_{max}$ values to 0.65 V and 110 mW cm^{-2}, respectively. The QPVA/annealed LaFeO$_3$ nanocomposite membrane had improved V$_{OC}$ (0.64 V) and P$_{max}$ (100 mW cm^{-2}) values. The performance was lower than that of the QPVA/CTAB-coated LaFeO$_3$ electrolyte but higher than that of the QPVA membrane. These results demonstrate that the small weight percentage of nanofiller in the QPVA matrix efficiently improved the alkaline cell performance.
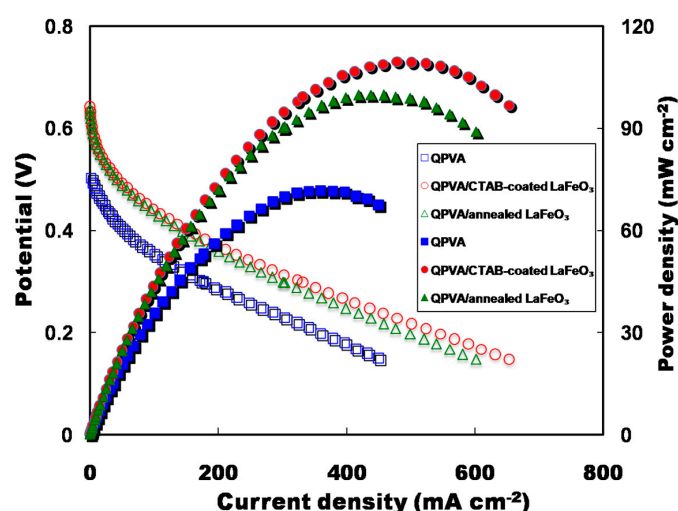
Figure 7. Direct alkaline methanol fuel cell voltage (**left** axis) and power density (**right** axis) as a function of current density using QPVA, QPVA/CTAB-coated LaFeO$_3$, and QPVA/annealed LaFeO$_3$ electrolytes at 30 °C and 4 M methanol.

The first reason for the performance improvement is the enhanced ionic conductivity of the electrolyte. The higher surface potential of the CTAB-coated nanoparticles strongly improved composite conductivity (the aforementioned chemical factor). The nanofiller presence decreased crystallinity of the nanocomposite membrane and increased fractional free volume (physical factor) to facilitate the transfer of hydroxyl ions [6,22,23,58,63]. Lo et al. employed a PVA/Fe_3O_4-CNT nanocomposite membrane and found a decrease in polymer crystallinity and improved ionic conductivity of membrane electrolytes and cell performance of alkaline fuel cells [20]. Similarly, Li et al. and Lioa et al. have demonstrated that QPVA/chitosan and QPVA/Q-chitosan composite membranes showed increased ionic conductivity, thereby improving methanol fuel cell performance [17,59]. The ionic conductivity of the QPVA/CTAB-coated nanoparticles is higher than that of other membranes due to suppressed crystallinity and high KOH uptake (Table 1), which improve cell performance.

The second reason for the power output enhancement is due to decreased methanol permeability. Both the CTAB-coated and annealed $LaFeO_3$ nanoparticles resulted in lower methanol permeability than the pure QPVA (Figure 5a). The pinhole-free composite (Figure 1j) with the CTAB-coated perovskite composite might form a better methanol barrier. The annealed $LaFeO_3$ composite contained cracks/defects (Figure 1n) which became methanol transport micro-channels. Thus, the CTAB-coated $LaFeO_3$ electrolyte generated a higher P_{max} than the annealed sample at the same operating temperature.

The effects of methanol concentration on alkaline fuel cell performance were studied by varying the anode feeds (1 M, 2 M, and 4 M). The V_{OC} and P_{max} in the DAMFCs equipped with QPVA/CTAB-coated $LaFeO_3$ electrolyte were measured at 60 °C, as shown in Figure 8a,b. A V_{OC} of 0.66 V and P_{max} of 187 mW cm^{-2} were achieved for 1 M methanol feed using QPVA/CTAB-coated $LaFeO_3$ electrolytes. When increased to 2 M and 4 M methanol, the V_{OC} also increased, to 0.82 V and 0.81 V, respectively. The increase is due to the faster catalytic reaction at the electrodes and the good methanol-barrier membrane. The P_{max} values increased to 250 mW cm^{-2} and 272 mW cm^{-2} for the 2 M and 4 M methanol feeds, respectively. The ability to operate at 4 M methanol is advantageous, as other membranes are optimal for 1 M or 2 M methanol feed [20,73]. The results confirm that our developed QPVA/CTAB-coated $LaFeO_3$ membrane has good methanol barrier properties and integral structure. For the QPVA/annealed $LaFeO_3$ electrolyte, the V_{OC} and P_{max} increased with increasing methanol concentration from 1 M to 4 M, as shown in Figure 8c,d. The corresponding values were lower than those of the QPVA/CTAB-coated $LaFeO_3$ electrolyte due to lower conductivity (associated with lower surface potential, higher polymer crystallinity, and interfacial defects of the composite) and higher methanol permeability than the QPVA/CTAB-coated $LaFeO_3$ electrolyte.

The polarization curves for DAMFCs obtained using the QPVA/CTAB-coated $LaFeO_3$ nanocomposite electrolyte at different temperatures (30–60 °C) are shown in supplementary Figure S7. The V_{OC} and P_{max} values were 0.65 V and 109 mW cm^{-2} at 30 °C. When the temperature was raised to 60 °C, the V_{OC} (0.81 V) and P_{max} (272 mW cm^{-2}) increased rapidly. The increased V_{OC} was due to high catalytic activities at the electrodes at 60 °C. Raising the cell temperature can accelerate the electrochemical kinetics of the reduction reaction at the cathode and the oxidation reaction at the anode [8]. Therefore higher electrical currents (that is, more electrons) were generated at a certain voltage [59]. The increased ionic conductivity is also beneficial to reduce ohmic loss by raising the temperature, as discussed previously. When the temperature was further increased to 70 °C, the P_{max} (264 mW cm^{-2}) value slightly decreased, which might be due to membrane shrinkage or dehydration at the higher temperature [74]. In addition, the increased methanol diffusivity from the unreacted methanol could also crossover into the cathode. Increased methanol diffusion also reduced the P_{max} value as a result of mixed potential methanol oxidation at the cathode. Therefore, the P_{max} was slightly reduced at 70 °C. A cell temperature of 60 °C seems a more appropriate setting.
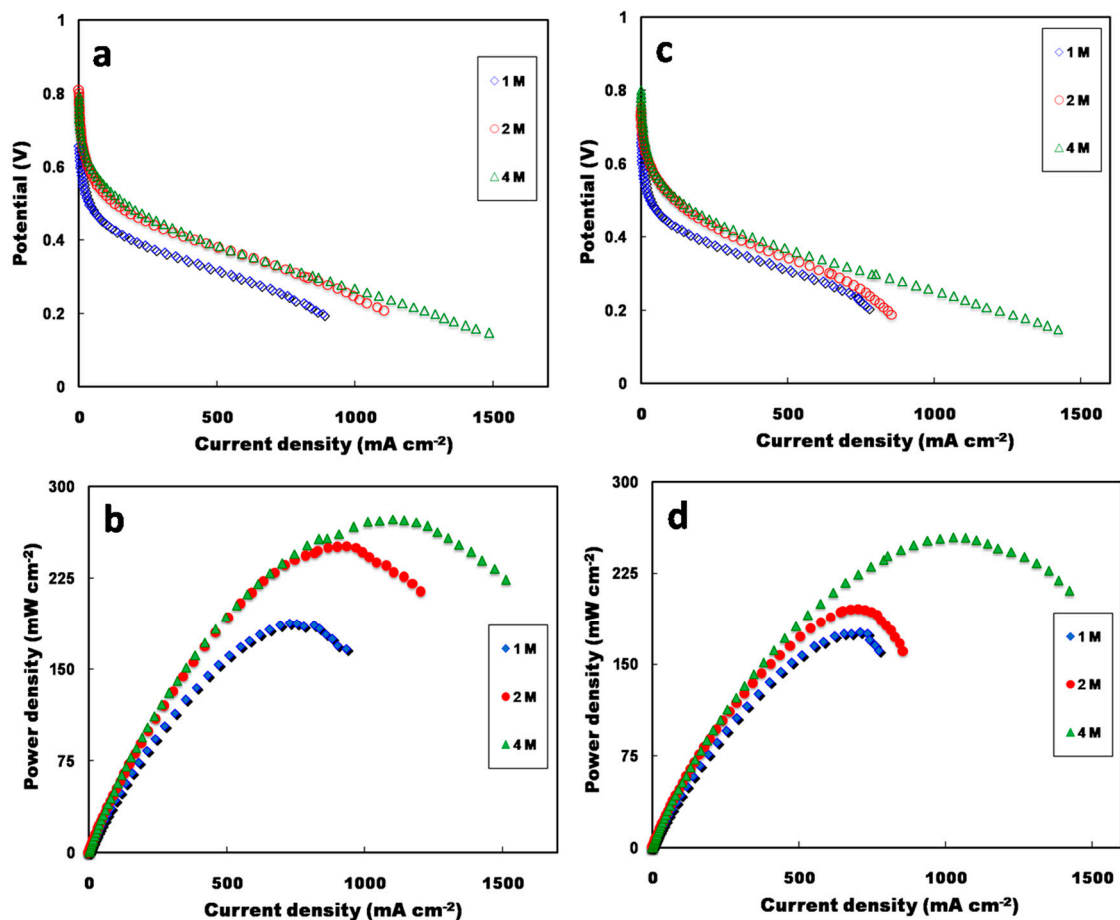
Figure 8. Effect of different concentrations of methanol feed on DAMFCs performance using KOH-doped nanocomposite electrolyte: (**a**) cell voltage; and (**b**) power density using QPVA/CTAB-coated LaFeO$_3$ as an electrolyte; (**c**) cell voltage; and (**d**) power density using QPVA/annealed LaFeO$_3$ as an electrolyte (cell temperature of 60 °C).

Based on the above tests, the optimal operating condition was fed with 4 M of methanol solution, cell temperature of 60 °C, and the use of the QPVA/CTAB-coated LaFeO$_3$ composite electrolyte. Many studies have proposed the incorporation of organic/inorganic nanofillers into a hydrophilic PVA matrix to enhance alkaline fuel cell performance, as shown in Table 2. The current results show a maximum P$_{max}$ of 272 mW cm^{-2} for the QPVA/CTAB-coated LaFeO$_3$ nanocomposite membrane due to its suppressed methanol permeability, with higher ionic conductivity compared with the QPVA/annealed LaFeO$_3$ nanocomposites. In this study, there was the low percentage of nanofillers (0.1 wt %) in QPVA matrix compared to other nanofillers reported in other research (Table 2). Moreover, we used low catalyst loadings in the anode (2 mg cm^{-1}) and cathode (1 mg cm^{-1}), which provided the advantage of low-cost DAMFC manufacturing. To our best knowledge, this P$_{max}$ output is the highest value of DAMFCs recorded [7,8,17–21,23,24,63,74–76].

Table 2. Comparison of maximum power densities for direct alkaline methanol fuel cells using various membrane electrolytes with conductivity and methanol permeability values. (Fuel cell catalyst loadings and temperatures are shown for reference).

Membrane Electrolyte	Nano-Filler Loading (wt %)	Cond. (mS cm^{-1})	Meth. Perm. ($\times 10^{-6}$ cm^2 s^{-1})	Operating Conditions				P$_{max}$ (mW cm^{-2})	References
				Anode Catalyst (Loading in mg cm^{-2})	Cathode Catalyst (Loading in mg cm^{-2})	Temp. (°C)	MeOH conc./ KOH conc.		
QPVA/PECH	25	8.8	46	Pt-Ru/C (4)	MnO$_2$/C (4)	25	2 M/4 M	22.3	Yang et al. [63]
QPVA/Al$_2$O$_3$	10	11	67	Pt-Ru/C (4)	MnO$_2$/C (4)	25	4 M/4 M	36.1	Yang et al. [21]
PVA/TiO$_2$	10	31	-^{a}	Pt-Ru/C (4)	Pt/C (4)	60	2 M/2 M	7.5	Yang et al. [19]
QPVA/CTAB-coated LaFeO$_3$	0.1	24	3.10	Pt-Ru/C (2)	Pt/C (1)	30	4 M/6 M	112	This work
QPVA/annealed LaFeO$_3$	0.1	14	3.50	Pt-Ru/C (2)	Pt/C (1)	30	4 M/6 M	100	This work
QPVA/Q-SiO$_2$	20	19	81	Pt-Ru/C (4)	MnO$_2$/C (4)	50	2 M/8 M	35.1	Yang et al. [7]
QPVA/chitosan	10	27	6.7	Pt-Ru/C (6)	Pt/C (5)	80	1 M/6 M	67	Li et al. [59]
QPVA/Q-chitosan	5	4.8	3.0	Pt-Ru/C (6)	Pt/C (5)	60	2 M/6 M	73	Liao et al. [17]
PVA/CNT	0.1	11.7	30	Pt-Ru/C (6)	Pt/C (5)	60	2 M/6 M	68.1	Lue et al. [8]
PVA/Fe$_3$O$_4$-CNT	10	48	8.9	Pt-Ru/C (6)	Pt/C (5)	60	2 M/6 M	87.8	Lo et al. [20]
Electrospun QPVA	-^{a}	41	5.2	Pt-Ru/C (6)	Pt/C (5)	60	2 M/6 M	54	Liao et al. [18]
QPVA/fumed silica	5	35	4.6	Pt-Ru/C (6)	Pt/C (5)	60	2 M/6 M	88.4	Kumar et al. [23]
QPVA/GO-Fe$_3$O$_4$	0.1	1.01	29	Pt-Ru/C (6)	Pt/C (5)	60	2 M/6 M	55.4	Lin et al. [24]
QPVA/CTAB-coated LaFeO$_3$	0.1	27	-^{a}	Pt-Ru/C (2)	Pt/C (1)	60	4 M/6 M	272	This work
QPVA/annealed LaFeO$_3$	0.1	18	-^{a}	Pt-Ru/C (2)	Pt/C (1)	60	4 M/6 M	254	This work

^{a} Not available.

3. Materials and Methods

3.1. Preparation of QPVA

The QPVA was prepared from PVA, glycidyltrimethyl ammonium chloride (GTMAC), and potassium hydroxide (KOH), as previously described [17].

3.2. Preparation of LaFeO$_3$ Nanoparticles and QPVA/LaFeO$_3$ Nanocomposite Membranes

A facile hydrothermal method was used to prepare the perovskite LaFeO$_3$ nanofillers. In a typical procedure, 2 mmol of Fe(NO$_3$)$_3$·6H$_2$O and 2 mmol of La(NO$_3$)$_3$·6H$_2$O were mixed in 40 mL of distilled (D.I.) water at ambient temperature. Similarly, 4 mmol of Na$_3$C$_6$H$_5$O$_7$ was dissolved in 20 mL of D.I. water by vigorous stirring. These two solutions were mixed together followed by the slow addition of surfactant CTAB under continuous stirring for 1 h at ambient temperature. The mixture solution was transferred into a 100 mL autoclave and held at 180 °C for 16 h. After completion of the hydrothermal process, the autoclave was cooled naturally to ambient temperature. The obtained precipitates were washed numerous times with ethanol and D.I. water using centrifugation. Afterwards, the sample was dried at 100 °C overnight in a hot air oven to produce CTAB-coated LaFeO$_3$ nanoparticles. A similar experimental procedure was followed to prepare pristine LaFeO$_3$ nanoparticles without the addition of CTAB surfactant. Portions of the CTAB-coated LaFeO$_3$ nanoparticles were annealed at 800 °C for 3 h using a muffle furnace in an air atmosphere with a heating ramp of 10 °C min^{-1} to tune their size, shape and crystalline properties.

An appropriate amount (0.1% loading by weight) of CTAB-coated or annealed LaFeO$_3$ nanoparticles were added to QPVA polymer solutions, which were degassed, cast, and dried in a vacuum oven at 60 °C overnight [17,18]. The thickness of the dry membrane was 50 ± 10 μm.

3.3. Physicochemical Properties of Nanoparticles and Nanocomposite Membranes

The morphology and microstructure of the nanoparticles and membrane composites were analysed using a transmission electron microscope (TEM), a high-resolution TEM (HRTEM), and a field emission scanning electron microscope (FESEM) equipped with an energy dispersive X-ray (EDX) detector [18,54,73]. The crystalline behaviours of the nanoparticles and composite membranes were assessed via X-ray diffraction (XRD) analyser and differential scanning calorimeter (DSC) [18,53,55]. The samples' chemical structures were analysed using X-ray photoelectron spectroscopy (XPS) and Fourier transform infrared spectroscopy (FTIR). Thermal stability was determined via thermo-gravimetric analysis (TGA) [54]. Particle zeta potentials were evaluated using a dynamic light scattering analyser (Zetasizer, 2000 HAS, Malvern, Worcestershire, UK) [77,78]. Particle suspension conductivities were measured using a conductivity meter while membrane conductivity was obtained from alternate-current impedance spectra [10]. The KOH uptake and partition, swelling ratio of in-plane and through-plane dimensions, ion-exchange capacity (IEC), methanol permeability, dissolution in water, and mechanical properties were assessed according to previously outlined procedures [18,20,53,55,59,76,79]. The fuel cell assembly and performance measurement methods have been described in previous work [56].

4. Conclusions

CTAB-coated LaFeO$_3$ nanoparticles were synthesized via the hydrothermal method, and a core-shell structure was observed with the CTAB surfactant at the outer layer. High crystallinity LaFeO$_3$ nanoparticles were prepared by annealing the pristine perovskite at 800 °C and the CTAB was completely degraded. The nanocomposite membranes were prepared by incorporating 0.1% LaFeO$_3$ nanoparticles (both CTAB-coated and annealed) into the QPVA matrix using a solution casting method. The nanocomposite membranes showed both suppressed dissolution in water and a reduced swelling ratio compared to the pristine QPVA membrane. The partial KOH uptake, IEC, and ionic conductivity of the QPVA/CTAB-coated LaFeO$_3$ membrane were higher than those of the QPVA/annealed LaFeO$_3$

and QPVA membranes. The QPVA/CTAB-coated LaFeO$_3$ composite showed higher ionic conductivity and lower methanol permeability than did the annealed sample. We suggest that the CTAB-coated LaFeO$_3$ provided three functions to the polymeric composite: increasing polymer free volume, ammonium group contributor, and plasticizer to enhance the interfacial compatibility. The P$_{max}$ of the QPVA/CTAB-coated LaFeO$_3$ nanocomposite membrane was found to be 272 mW cm^{-2} at 60 °C when fed with 4 M methanol and 6 M KOH as the anode feed. The power densities using this type of alkaline fuel cells were significantly higher than the existing data in the literature. These findings suggest that QPVA/CTAB-coated LaFeO$_3$ is a promising hydroxide-conducting membrane for DAMFC applications.

References

1. Wang, Y.-J.; Zhao, N.; Fang, B.; Li, H.; Bi, X.T.; Wang, H. Carbon-supported Pt-based alloy electrocatalysts for the oxygen reduction reaction in polymer electrolyte membrane fuel cells: Particle size, shape, and composition manipulation and their impact to activity. *Chem. Rev.* **2015**, *115*, 3433–3467. [CrossRef] [PubMed]

2. García-Cruz, L.; Casado-Coterillo, C.; Iniesta, J.; Montiel, V.; Irabien, Á. Chitosan: Poly(vinyl) alcohol composite alkaline membrane incorporating organic ionomers and layered silicate materials into a PEM electrochemical reactor. *J. Membr. Sci.* **2016**, *498*, 395–407. [CrossRef]

3. Si, Z.; Qiu, L.; Dong, H.; Gu, F.; Li, Y.; Yan, F. Effects of substituents and substitution positions on alkaline stability of imidazolium cations and their corresponding anion-exchange membranes. *ACS Appl. Mater. Interfaces* **2014**, *6*, 4346–4355. [CrossRef] [PubMed]

4. Zhou, T.; Shao, R.; Chen, S.; He, X.; Qiao, J.; Zhang, J. A review of radiation-grafted polymer electrolyte membranes for alkaline polymer electrolyte membrane fuel cells. *J. Power Sources* **2015**, *293*, 946–975. [CrossRef]

5. Li, X.; Yu, Y.; Meng, Y. Novel Quaternized Poly(arylene ether sulfone)/nano-ZrO$_2$ composite anion exchange membranes for alkaline fuel cells. *ACS Appl. Mater. Interfaces* **2013**, *5*, 1414–1422. [CrossRef] [PubMed]

6. Lue, S.J.; Mahesh, K.P.O.; Wang, W.-T.; Chen, J.-Y.; Yang, C.-C. Permeant transport properties and cell performance of potassium hydroxide doped poly(vinyl alcohol)/fumed silica nanocomposites. *J. Membr. Sci.* **2011**, *367*, 256–264. [CrossRef]

7. Yang, C.-C.; Chiu, S.-S.; Kuo, S.-C.; Liou, T.-H. Fabrication of anion-exchange composite membranes for alkaline direct methanol fuel cells. *J. Power Sources* **2012**, *199*, 37–45. [CrossRef]

8. Lue, S.J.; Pan, W.-H.; Chang, C.-M.; Liu, Y.-L. High-performance direct methanol alkaline fuel cells using potassium hydroxide-impregnated polyvinyl alcohol/carbon nano-tube electrolytes. *J. Power Sources* **2012**, *202*, 1–10. [CrossRef]

9. Wang, Y.-J.; Qiao, J.; Baker, R.; Zhang, J. Alkaline polymer electrolyte membranes for fuel cell applications. *Chem. Soc. Rev.* **2013**, *42*, 5768–5787. [CrossRef] [PubMed]

10. Lue, S.J.; Wang, W.-T.; Mahesh, K.P.O.; Yang, C.-C. Enhanced performance of a direct methanol alkaline fuel cell (DMAFC) using a polyvinyl alcohol/fumed silica/KOH electrolyte. *J. Power Sources* **2010**, *195*, 7991–7999. [CrossRef]

11. Sheibley, D.W.; Manzo, M.A. Polyvinyl Alcohol Membrances as Alkaline Battery Separetors. Available online: http://ntrs.nasa.gov/archive/nasa/casi.ntrs.nasa.gov/19830001865.pdf (accessed on 1 January 1982).

12. Fang, J.; Qiao, J.; Wilkinson, D.P.; Zhang, J. *Electrochemical Polymer Electrolyte Membranes*; CRC Press, Taylor & Francis Group: London, UK, 2015.

13. Fu, J.; Lee, D.U.; Hassan, F.M.; Yang, L.; Bai, Z.; Park, M.G.; Chen, Z. Flexible high-energy polymer-electrolyte-based rechargeable zinc–air batteries. *Adv. Mater.* **2015**, *27*, 5617–5622. [CrossRef] [PubMed]

14. Fu, J.; Qiao, J.; Wang, X.; Ma, J.; Okada, T. Alkali doped poly(vinyl alcohol) for potential fuel cell applications. *Synth. Met.* **2010**, *160*, 193–199. [CrossRef]

15. Stoševski, I.; Krstić, J.; Vokić, N.; Radosavljević, M.; Popović, Z.K.; Miljanić, Š. Improved Poly(vinyl alcohol) (PVA) based matrix as a potential solid electrolyte for electrochemical energy conversion devices, obtained by gamma irradiation. *Energy* **2015**, *90*, 595–604. [CrossRef]

16. Fu, J.; Qiao, J.; Lv, H.; Ma, J.; Yuan, X.-Z.; Wang, H. Alkali doped poly(vinyl alcohol) (PVA) for anion-exchange membrane fuel cells: Ionic conductivity, chemical stability and FT-IR characterizations. *ECS Trans.* **2010**, *25*, 15–23.

17. Liao, G.-M.; Yang, C.-C.; Hu, C.-C.; Pai, Y.-L.; Lue, S.J. Novel quaternized polyvinyl alcohol/quaternized chitosan nano-composite as an effective hydroxide-conducting electrolyte. *J. Membr. Sci.* **2015**, *485*, 17–29. [CrossRef]

18. Liao, G.-M.; Li, P.-C.; Lin, J.-S.; Ma, W.-T.; Yu, B.-C.; Li, H.-Y.; Liu, Y.-L.; Yang, C.-C.; Shih, C.-M.; Lue, S.J. Highly conductive quasi-coaxial electrospun quaternized polyvinyl alcohol nanofibers and composite as high-performance solid electrolytes. *J. Power Sources* **2016**, *304*, 136–145. [CrossRef]

19. Yang, C.-C. Synthesis and characterization of the cross-linked PVA/TiO$_2$ composite polymer membrane for alkaline DMFC. *J. Membr. Sci.* **2007**, *288*, 51–60. [CrossRef]

20. Lo, C.-F.; Wu, J.-F.; Li, H.-Y.; Hung, W.-S.; Shih, C.-M.; Hu, C.-C.; Liu, Y.-L.; Lue, S.J. Novel polyvinyl alcohol nanocomposites containing carbon nano-tubes with Fe$_3$O$_4$ pendants for alkaline fuel cell applications. *J. Membr. Sci.* **2013**, *444*, 41–49. [CrossRef]

21. Yang, C.-C.; Chiu, S.-J.; Chien, W.-C.; Chiu, S.-S. Quaternized poly(vinyl alcohol)/alumina composite polymer membranes for alkaline direct methanol fuel cells. *J. Power Sources* **2010**, *195*, 2212–2219. [CrossRef]

22. Merle, G.; Wessling, M.; Nijmeijer, K. Anion exchange membranes for alkaline fuel cells: A review. *J. Membr. Sci.* **2011**, *377*, 1–35. [CrossRef]

23. Rajesh Kumar, S.; Juan, C.-H.; Liao, G.-M.; Lin, J.-S.; Yang, C.-C.; Ma, W.-T.; You, J.-H.; Jessie Lue, S. Fumed silica nanoparticles incorporated in quaternized poly(vinyl alcohol) nanocomposite membrane for enhanced power densities in direct alcohol alkaline fuel cells. *Energies* **2016**, *9*, 15. [CrossRef]

24. Lin, J.-S.; Ma, W.-T.; Shih, C.-M.; Yu, B.-C.; Teng, L.-W.; Wang, Y.-C.; Cheng, K.-W.; Chiu, F.-C.; Lue, S. Reorientation of magnetic graphene oxide nanosheets in crosslinked quaternized polyvinyl alcohol as effective solid electrolyte. *Energies* **2016**, *9*, 1003. [CrossRef]

25. Mehta, S.; Kumar, S.; Chaudhary, S.; Bhasin, K.; Gradzielski, M. Evolution of ZnS nanoparticles via facile CTAB aqueous micellar solution route: A study on controlling parameters. *Nanoscale Res. Lett.* **2008**, *4*, 17. [CrossRef] [PubMed]

26. Su, H.; Jing, L.; Shi, K.; Yao, C.; Fu, H. Synthesis of large surface area LaFeO$_3$ nanoparticles by SBA-16 template method as high active visible photocatalysts. *J. Nanopart. Res.* **2010**, *12*, 967–974. [CrossRef]

27. Ekrami-Kakhki, M.-S.; Yavari, Z.; Saffari, J.; Ekrami-Kakhki, S.A. Perovskite-type LaFeO$_3$ and LaFeO$_3$-CNTs nanocrystals as active anode for methanol oxidation in alkaline solutions. *J. Electr. Eng.* **2016**, *4*, 88–99.

28. Xuefeng Zhu, W.Y. *Mixed Conducting Ceramic Membranes: Fundamentals, Materials and Applications*; Springer: Berlin, Germany, 2017; Volume 1, pp. 1–367.

29. Royer, S.; Duprez, D.; Can, F.; Courtois, X.; Batiot-Dupeyrat, C.; Laassiri, S.; Alamdari, H. Perovskites as substitutes of noble metals for heterogeneous catalysis: Dream or reality. *Chem. Rev.* **2014**, *114*, 10292–10368. [CrossRef] [PubMed]

30. Thirumalairajan, S.; Girija, K.; Mastelaro, V.R.; Ponpandian, N. Investigation on magnetic and electric properties of morphologically different perovskite LaFeO$_3$ nanostructures. *J. Mater. Sci. Mater. Electron.* **2015**, *26*, 8652–8662. [CrossRef]

31. Mizusaki, J.; Yoshihiro, M.; Yamauchi, S.; Fueki, K. Nonstoichiometry and defect structure of the perovskite-type oxides La$_{1-x}$Sr$_x$FeO$_{3-\circ}$. *J. Solid State Chem.* **1985**, *58*, 257–266. [CrossRef]

32. Spinicci, R.; Tofanari, A.; Delmastro, A.; Mazza, D.; Ronchetti, S. Catalytic properties of stoichiometric and non-stoichiometric LaFeO$_3$ perovskite for total oxidation of methane. *Mater. Chem. Phys.* **2002**, *76*, 20–25. [CrossRef]

33. Tsipis, E.V.; Kiselev, E.A.; Kolotygin, V.A.; Waerenborgh, J.C.; Cherepanov, V.A.; Kharton, V.V. Mixed conductivity, Mossbauer spectra and thermal expansion of (La,Sr)(Fe,Ni)O$_{3-\delta}$ perovskites. *Solid State Ion.* **2008**, *179*, 2170–2180. [CrossRef]

34. Dai, Z.; Lee, C.-S.; Kim, B.-Y.; Kwak, C.-H.; Yoon, J.-W.; Jeong, H.-M.; Lee, J.-H. Honeycomb-like periodic porous LaFeO$_3$ thin film chemiresistors with enhanced gas-sensing performances. *ACS Appl. Mater. Interfaces* **2014**, *6*, 16217–16226. [CrossRef] [PubMed]

35. Unemoto, A.; Kaimai, A.; Sato, K.; Kitamura, N.; Yashiro, K.; Matsumoto, H.; Mizusaki, J.; Amezawa, K.; Kawada, T. High-temperature protonic conduction in LaFeO$_3$–SrFeO$_{3-\delta}$–SrZrO$_3$ solid solutions. *J. Electrochem. Soc.* **2011**, *158*, B180–B188. [CrossRef]

36. Cordero, F.; Craciun, F.; Trequattrini, F. Ionic mobility and phase transitions in perovskite oxides for energy application. *Challenges* **2017**, *8*, 5. [CrossRef]

37. Chen, D.; Chen, C.; Baiyee, Z.M.; Shao, Z.; Ciucci, F. Nonstoichiometric oxides as low-cost and highly-efficient oxygen reduction/evolution catalysts for low-temperature electrochemical devices. *Chem. Rev.* **2015**, *115*, 9869–9921. [CrossRef] [PubMed]

38. Dhinesh Kumar, R.; Jayavel, R. Facile hydrothermal synthesis and characterization of LaFeO$_3$ nanospheres for visible light photocatalytic applications. *J. Mater. Sci. Mater. Electron.* **2014**, *25*, 3953–3961. [CrossRef]

39. Huang, K.; Yuan, L.; Feng, S. Crystal facet tailoring arts in perovskite oxides. *Inorgan. Chem. Front.* **2015**, *2*, 965–981. [CrossRef]

40. Liu, Y.; Tourbin, M.; Lachaize, S.; Guiraud, P. Silica nanoparticles separation from water: Aggregation by cetyltrimethylammonium bromide (CTAB). *Chemosphere* **2013**, *92*, 681–687. [CrossRef] [PubMed]

41. Wang, H.; Zhao, X.; Meng, W.; Wang, P.; Wu, F.; Tang, Z.; Han, X.; Giesy, J.P. Cetyltrimethylammonium bromide-coated Fe$_3$O$_4$ magnetic nanoparticles for analysis of 15 trace polycyclic aromatic hydrocarbons in aquatic environments by ultraperformance, liquid chromatography with fluorescence detection. *Anal. Chem.* **2015**, *87*, 7667–7675. [CrossRef] [PubMed]

42. Cheng, W.; Dong, S.; Wang, E. Synthesis and Self-Assembly of Cetyltrimethylammonium Bromide-Capped Gold Nanoparticles. *Langmuir* **2003**, *19*, 9434–9439. [CrossRef]

43. Wang, H.-Q.; Wei, X.; Wang, K.-X.; Chen, J.-S. Controlled synthesis of magnetic Pd/Fe$_3$O$_4$ spheres via an ethylenediamine-assisted route. *Dalton Trans.* **2012**, *41*, 3204–3208. [CrossRef] [PubMed]

44. Feng, J.; Liu, T.; Xu, Y.; Zhao, J.; He, Y. Effects of PVA content on the synthesis of LaFeO$_3$ via sol–gel route. *Ceram. Int.* **2011**, *37*, 1203–1207. [CrossRef]

45. Hudspeth, J.M.; Stewart, G.A.; Studer, A.J.; Goossens, D.J. Crystal and magnetic structures in Perovskite-related (*x* = 0.2, 0.33). *J. Phys. Chem. Solids* **2011**, *72*, 1543–1547. [CrossRef]

46. Thirumalairajan, S.; Girija, K.; Mastelaro, V.R.; Ponpandian, N. Photocatalytic degradation of organic dyes under visible light irradiation by floral-like LaFeO$_3$ nanostructures comprised of nanosheet petals. *New J. Chem.* **2014**, *38*, 5480–5490. [CrossRef]

47. Tesquet, G.; Faye, J.; Hosoglu, F.; Mamede, A.-S.; Dumeignil, F.; Capron, M. Ethanol reactivity over La$_{1+x}$FeO$_{3+\delta}$ perovskites. *Appl. Catal. A Gen.* **2016**, *511*, 141–148. [CrossRef]

48. Li, S.; Jin, W.; Xu, N.; Shi, J. Synthesis and oxygen permeation properties of La$_{0.2}$Sr$_{0.8}$Co$_{0.2}$Fe$_{0.8}$O$_{3-\delta}$ membranes. *Solid State Ion.* **1999**, *124*, 161–170. [CrossRef]

49. Pishahang, M.; Bakken, E.; Stølen, S.; Thomas, C.I.; Dahl, P.I. Oxygen non-stoichiometry, redox thermodynamics, and structure of LaFe$_{1-x}$Co$_x$O$_{3-\delta}$. *Ionics* **2013**, *19*, 869–878. [CrossRef]

50. Delmastro, A.; Mazza, D.; Ronchetti, S.; Vallino, M.; Spinicci, R.; Brovetto, P.; Salis, M. Synthesis and characterization of non-stoichiometric LaFeO$_3$ perovskite. *Mater. Sci. Eng. B* **2001**, *79*, 140–145. [CrossRef]

51. Li, P.; Hu, X.; Zhang, L.; Dai, H.; Zhang, L. Sol-gel nanocasting synthesis of patterned hierarchical LaFeO$_3$ fibers with enhanced catalyticCO oxidation activity. *Nanoscale* **2011**, *3*, 974–976. [CrossRef] [PubMed]

52. Lee, W.-Y.; Yun, H.J.; Yoon, J.-W. Characterization and magnetic properties of LaFeO$_3$ nanofibers synthesized by electrospinning. *J. Alloys Compd.* **2014**, *583*, 320–324. [CrossRef]

53. Lue, S.J.; Lee, D.-T.; Chen, J.-Y.; Chiu, C.-H.; Hu, C.-C.; Jean, Y.C.; Lai, J.-Y. Diffusivity enhancement of water vapor in poly(vinyl alcohol)–fumed silica nano-composite membranes: Correlation with polymer crystallinity and free-volume properties. *J. Membr. Sci.* **2008**, *325*, 831–839. [CrossRef]

54. Pan, W.-H.; Lue, S.J.; Chang, C.-M.; Liu, Y.-L. Alkali doped polyvinyl alcohol/multi-walled carbon nano-tube electrolyte for direct methanol alkaline fuel cell. *J. Membr. Sci.* **2011**, *376*, 225–232. [CrossRef]

55. Jessie Lue, S.; Chen, J.Y.; Ming Yang, J. Crystallinity and stability of poly(vinyl alcohol)-fumed silica mixed matrix membranes. *J. Macromol. Sci. Part B* **2007**, *47*, 39–51.

56. Wu, J.-F.; Lo, C.-F.; Li, L.-Y.; Li, H.-Y.; Chang, C.-M.; Liao, K.-S.; Hu, C.-C.; Liu, Y.-L.; Lue, S.J. Thermally stable polybenzimidazole/carbon nano-tube composites for alkaline direct methanol fuel cell applications. *J. Power Sources* **2014**, *246*, 39–48. [CrossRef]

57. Emmanuel, K.; Cheng, C.; Erigene, B.; Mondal, A.N.; Hossain, M.M.; Khan, M.I.; Afsar, N.U.; Liang, G.; Wu, L.; Xu, T. Imidazolium functionalized anion exchange membrane blended with PVA for acid recovery via diffusion dialysis process. *J. Membr. Sci.* **2016**, *497*, 209–215. [CrossRef]

58. Huang, C.-Y.; Lin, J.-S.; Pan, W.-H.; Shih, C.-M.; Liu, Y.-L.; Lue, S.J. Alkaline direct ethanol fuel cell performance using alkali-impregnated polyvinyl alcohol/functionalized carbon nano-tube solid electrolytes. *J. Power Sources* **2016**, *303*, 267–277. [CrossRef]

59. Li, P.-C.; Liao, G.M.; Kumar, S.R.; Shih, C.-M.; Yang, C.-C.; Wang, D.-M.; Lue, S.J. Fabrication and Characterization of Chitosan Nanoparticle-Incorporated Quaternized Poly(Vinyl Alcohol) Composite Membranes as Solid Electrolytes for Direct Methanol Alkaline Fuel Cells. *Electrochim. Acta* **2016**, *187*, 616–628. [CrossRef]

60. Wang, B.-Y.; Lin, H.-K.; Liu, N.-Y.; Mahesh, K.P.O.; Lue, S.J. Cell performance modeling of direct methanol fuel cells using proton-exchange solid electrolytes: Effective reactant diffusion coefficients in porous diffusion layers. *J. Power Sources* **2013**, *227*, 275–283. [CrossRef]

61. Gi Hong, J.; Glabman, S.; Chen, Y. Effect of inorganic filler size on electrochemical performance of nanocomposite cation exchange membranes for salinity gradient power generation. *J. Membr. Sci.* **2015**, *482*, 33–41. [CrossRef]

62. Watanabe, H.; Takahashi, H.; Takeguchi, T.; Yamanaka, T.; Ueda, W. Performance of Solid Alkaline Fuel Cells Employing Layered Perovskite-Type Oxides as Electrolyte. *ECS Trans.* **2010**, *33*, 1825–1829.

63. Yang, C.-C. Alkaline direct methanol fuel cell based on a novel anion-exchange composite polymer membrane. *J. Appl. Electrochem.* **2012**, *42*, 305–317. [CrossRef]

64. Thirumalairajan, S.; Girija, K.; Ganesh, V.; Mangalaraj, D.; Viswanathan, C.; Ponpandian, N. Novel Synthesis of $LaFeO_3$ Nanostructure Dendrites: A Systematic Investigation of Growth Mechanism, Properties, and Biosensing for Highly Selective Determination of Neurotransmitter Compounds. *Cryst. Growth Des.* **2013**, *13*, 291–302. [CrossRef]

65. Mihai, O.; Raaen, S.; Chen, D.; Holmen, A. Preparation of stable cubic $LaFeO_3$ nanoparticles using carbon nanotubes as templates. *J. Mater. Chem. A* **2013**, *1*, 7006–7011. [CrossRef]

66. Jing, L.; Qu, Y.; Su, H.; Yao, C.; Fu, H. Synthesis of High-Activity TiO_2-Based Photocatalysts by Compounding a Small Amount of Porous Nanosized $LaFeO_3$ and the Activity-Enhanced Mechanisms. *J. Phys. Chem. C* **2011**, *115*, 12375–12380. [CrossRef]

67. Wang, J.; Huang, S.-p.; Hu, K.; Zhou, K.-c.; Sun, H. Effect of cetyltrimethylammonium bromide on morphology and porous structure of mesoporous hydroxyapatite. *Trans. Nonferr. Met. Soc. China* **2015**, *25*, 483–489. [CrossRef]

68. Micellisation of Cetyltrimethyl Ammonium Bromide in Aqueous-Organic Media. Available online: http://astonjournals.com/manuscripts/Vol2012/CSJ-52_Vol2012.pdf (accessed on 2 March 2017).

69. Krevelen, D.W.V. *Properties of Polymers: Their Correlation with Chemical Structure; Their Numerical Estimation and Prediction from Additive Group Contributions*, 3rd ed.; Elsevier Science B.V.: Amsterdam, The Netherlands, 1990.

70. Ramasubramanian, K.; Severance, M.A.; Dutta, P.K.; Ho, W.S.W. Fabrication of zeolite/polymer multilayer composite membranes for carbon dioxide capture: Deposition of zeolite particles on polymer supports. *J. Coll. Interface Sci.* **2015**, *452*, 203–214. [CrossRef] [PubMed]

71. Wang, Y.; Han, Q.; Zhou, Q.; Du, X.; Xue, L. Molecular sieving effect of zeolites on the properties of PVA based composite membranes for total heat recovery in ventilation systems. *RSC Adv.* **2016**, *6*, 66767–66773. [CrossRef]

72. Yang, C.; Wang, S.; Ma, W.; Jiang, L.; Sun, G. Comparison of alkaline stability of quaternary ammonium- and 1,2-methylimidazolium-based alkaline anion exchange membranes. *J. Membr. Sci.* **2015**, *487*, 12–18. [CrossRef]

73. Lue, S.J.; Pai, Y.-L.; Shih, C.-M.; Wu, M.-C.; Lai, S.-M. Novel bilayer well-aligned Nafion/graphene oxide composite membranes prepared using spin coating method for direct liquid fuel cells. *J. Membr. Sci.* **2015**, *493*, 212–223. [CrossRef]

74. Chien, H.-C.; Tsai, L.-D.; Huang, C.-P.; Kang, C.-y.; Lin, J.-N.; Chang, F.-C. Sulfonated graphene oxide/Nafion composite membranes for high-performance direct methanol fuel cells. *Int. J. Hydrogen Energy* **2013**, *38*, 13792–13801. [CrossRef]

75. Yang, J.-M.; Wang, N.-C.; Chiu, H.-C. Preparation and characterization of poly(vinyl alcohol)/sodium alginate blended membrane for alkaline solid polymer electrolytes membrane. *J. Membr. Sci.* **2014**, *457*, 139–148. [CrossRef]

76. Li, L.-Y.; Yu, B.-C.; Shih, C.-M.; Lue, S.J. Polybenzimidazole membranes for direct methanol fuel cell: Acid-doped or alkali-doped? *J. Power Sources* **2015**, *287*, 386–395. [CrossRef]

77. Chou, F.-Y.; Lai, J.-Y.; Shih, C.-M.; Tsai, M.-C.; Lue, S.J. In vitro biocompatibility of magnetic thermo-responsive nanohydrogel particles of poly(N-isopropylacrylamide-co-acrylic acid) with Fe_3O_4 cores: Effect of particle size and chemical composition. *Coll. Surf. B Biointerfaces* **2013**, *104*, 66–74. [CrossRef] [PubMed]

78. Lue, S.J.; Chen, B.-W.; Shih, C.-M.; Chou, F.-Y.; Lai, J.-Y.; Chiu, W.-Y. Micron- and Nano-sized Poly(N-isopropylacrylamide-co-acrylic acid) Latex Syntheses and Their Applications for Controlled Drug Release. *J. Nanosci. Nanotechnol.* **2013**, *13*, 5305–5315. [CrossRef] [PubMed]

79. Huang, C.-C.; Liu, Y.-L.; Pan, W.-H.; Chang, C.-M.; Shih, C.-M.; Chu, H.-Y.; Chien, C.-H.; Juan, C.-H.; Lue, S.J. Direct borohydride fuel cell performance using hydroxide-conducting polymeric nanocomposite electrolytes. *J. Polym. Sci. Part B Polym. Phys.* **2013**, *51*, 1779–1789. [CrossRef]